ELSEVIER

Remote Sensing of Environment 81 (2002) 1–18

Remote Sensing of Environment

www.elsevier.com/locate/rse

Effects of spectral response function on surface reflectance and NDVI measured with moderate resolution satellite sensors

Alexander P. Trishchenko[a,*], Josef Cihlar[a], Zhanqing Li[a,b]

[a]*Canada Centre for Remote Sensing, Natural Resources Canada, 588 Booth Street Ottawa, Ontario, Canada K1A 0Y7*
[b]*University of Maryland, ESSIC, College Park, MD, 20742, USA*

Received 14 June 2001; received in revised form 15 October 2001; accepted 15 October 2001

Abstract

We report the results of a modeling study on the sensitivity of normalized difference vegetation index (NDVI) and surface reflectance to differences in instrument spectral response functions (SRF) for various Advanced Very High Resolution Radiometers (AVHRR) onboard the National Oceanic and Atmospheric Administration's (NOAA) satellites NOAA-6–16 as well as the Moderate Resolution Imaging Spectroradiometer (MODIS), the Vegetation sensor (VGT), and the Global Imager (GLI). Modeling results were validated against real satellite observations employing AVHRR/NOAA-14 and -15 and MODIS, with a very good agreement. It is shown that for identical atmospheric state and similar surface spectral reflectance, the NDVI and spectral reflectances are sensitive to the sensor's SRF. Relative to a reference SRF for AVHRR/NOAA-9, the differences in reflectance among the AVHRRs range from −25% to 12% for visible channel (red) and from −2% to 4% for near-infrared (NIR) channel. Absolute change in NDVI among various AVHRRs ranged from −0.02 to 0.06. The most significant difference was observed for the AVHRR/3. Consistent results were obtained with the AVHRR sensors aboard the following afternoon satellites: NOAA-9, -11, and -12, whereas important discrepancies were found for other AVHRRs aboard NOAA-6 and -10 and especially those launched more recently (NOAA-15 and -16). Reflectance and NDVI measured by MODIS channels 1 and 2 also exhibit significant differences (up to 30–40%) relative to AVHRR. GLI and VGT have some specific features that should be taken into account when intercomparing surface or top of the atmosphere (TOA) reflectance as well as NDVI. Sensitivity of the SRF effect to variable atmospheric state (water vapor, aerosol, and ozone) was also investigated. Polynomial approximations are provided for bulk spectral correction with respect to AVHRR/NOAA-9.

Keywords: Satellite; Surface reflectance; AVHRR; MODIS; GLI; VGT; NDVI; Spectral response function; Spectral correction; Global change detection

1. Introduction

Satellite observation is a convenient and feasible tool for global monitoring of atmospheric and terrestrial environment due to frequent and global coverage. Among various satellite sensors, the Advanced Very High Resolution Radiometer (AVHRR) onboard the National Oceanic and Atmospheric Administration's (NOAA) polar orbiting satellites has the longest record for research and application (Cracknell, 1997). There are three series of the AVHRR instruments. The four-channel radiometers AVHRR/1 were launched onboard the Tiros-N and NOAA-6, -8, and -10. The five-channel radiometers AVHRR/2 were deployed on the platforms NOAA-7, -9, -11, -12, and -14 followed by a six-channel radiometer AVHRR/3 onboard the NOAA-15 and -16.

The range of AVHRR data applications is very broad. To name a few, e.g., the visible and near-infrared (NIR) channels of AVHRR are used for retrieving cloud parameters (Rossow, 1989), solar radiation budget (Hucek & Jacobowitz, 1995), determination of absorbed photosynthetically active radiation (APAR; Li, Moreau, & Cihlar, 1997), and retrievals of aerosol optical depth (AOD; Stowe, Ignatov, & Singh, 1997) and other parameters (Gutman, Csiszar, & Romanov, 2000; Nakajima, Higurashi, Kawamoto, & Penner, 2001). One of the most important applications of the AVHRR thermal channels lies in estimation of global sea surface temperature (SST; Reynolds & Smith, 1993). The thermal channels are also used for determining

* Corresponding author. Tel.: +1-613-995-5787; fax: +1-613-947-1406.
E-mail address: trichtch@ccrs.nrcan.gc.ca (A.P. Trishchenko).

0034-4257/01/$ – see front matter
PII: S0034-4257(01)00328-5

land surface temperature and emissivity (Qin & Karnieli, 1999). Thermal AVHRR channels in combination with channels 1 and 2 are employed for forest fire detection and monitoring (Li, Nadon, & Cihlar, 2000).

An important application of AVHRR solar channels is the retrieval of surface reflectance to determine different land surface parameters such as surface cover type (Cihlar et al., in press), normalized difference vegetation index (NDVI; Kidwell, 1994), leaf area index (LAI; Chen, Rich, Gower, Norman, & Plummer, 1997), and other surface characteristics. New opportunities for global monitoring of terrestrial ecosystem are unfolding with the availability of Moderate Resolution Imaging Spectroradiometer (MODIS) data.

The processing of satellite data involves many steps. The final purpose of satellite data processing in land surface studies is to obtain the systematic maps of various quantitative physical parameters corrected for the intervening effect of atmosphere, effect of varying observational geometry, and specific sensor properties. Some of these corrections can be done quite accurately, like correction for Raleigh molecular scattering. Nonetheless, most of them may be implemented with some uncertainty due to limited knowledge of input information.

The important processing step is the data calibration. Despite numerous efforts, the results often vary among different investigators (Brest, Rossow, & Roiter, 1997; Gutman, 1999; Masonis & Warren, 2001; Rao & Chen, 1999; Tahnk & Coakley, 2001). Accurate calibration requires continuos monitoring of the gain and offset due to degradation of sensor sensitivity with time. The degradation may not necessarily be a linear function of time (Tahnk & Coakley, 2001). It is commonly agreed that for satellite sensors lacking onboard calibration in solar spectrum, the total relative uncertainties of calibration are within 5% (Rossow & Schiffer, 1999). An essential part of this uncertainty is related to the effect of spectral response function (SRF), when it is not accounted for properly during vicarious calibration or sensor intercalibration (Teillet et al., 2001).

Variable sun and observational geometry induces another source of systematic noise (Gutman, Gruber, Tarpley, & Taylor, 1989; Li, Cihlar, Zheng, Moreau, & Ly, 1996). This angular effect is a combination of anisotropic reflective properties of the atmosphere and land surface. The effect must be accounted for in long-term studies of satellite data to obtain unbiased results (Cihlar et al., 1998; Gutman, 1999). This is achieved by normalizing satellite image to common geometry using empirical anisotropic factors. They are derived either from sequence of satellite scenes collected over long period of time (Cihlar et al., 1998; Trishchenko, Li, Park, & Cihlar, in press) or from special directional observations, like those ones from POLDER or MISR instruments (Csiszar, Gutman, Romanov, Leroy, & Hautecoeur, 2001). Neglecting angular correction in the AVHRR data processing, for example, may introduce biases in composite coarse resolution long-term reflectance datasets of the order of 1–2% depending on spectral band and surface type (Gutman, 1999). The effect becomes more significant (5–10%) for solar zenith angles (SZA) greater than 55°.

Numerous vegetation indices have been developed to monitor the state of vegetation from spaceborne instruments (Bannari, Morin, & Bonn, 1995). They were constructed to diminish atmospheric contamination, mitigate the influence of soil spectral reflectance signatures, or emphasize certain features of vegetation conditions. The set of advanced vegetation indices optimised for upcoming sensors is discussed by Gobron, Pinty, Verstraete, and Widlowski (2000). Nevertheless, NDVI remains the basic vegetation index most widely employed for global monitoring of vegetation. It is defined as the following ratio:

$$\mathrm{NDVI} = \frac{\rho^{\mathrm{NIR}} - \rho^{\mathrm{red}}}{\rho^{\mathrm{NIR}} + \rho^{\mathrm{red}}},$$

where ρ^{NIR} and ρ^{red} are reflectances for visible (red) and NIR spectral bands.

Attempts have been made to use the AVHRR data for long-term monitoring of land reflectances and vegetation indices (Cihlar et al., in press; Gutman, 1999; Kaufman et al., 2000). These and other studies on long-term monitoring are motivated by the availability of quality AVHRR time series for the period of nearly 20 years. Although the construction and characteristics of all AVHRR instruments are quite similar, they are not identical among all missions. Consequently, the effect of varying spectral response may create an artificial noise imposed upon a subtle natural variability. This artifact should be examined thoroughly before comparing data between different missions to determine possible changes in satellite climatic records. So far, the effects of SRFs have not been considered carefully in such studies. Some influence of the spectral characteristic of the satellite sensors on remote sensing of vegetation indices has been studied for forested regions (Teillet, Staenz, & Williams, 1997) and during vicarious calibrations procedures (Teillet et al., 2001). Nevertheless, systematic characterisation of these effects for various representative surface spectral signatures on a global scale and for all AVHRR sensors has not been addressed properly. Analysis of long-term satellite products from various missions may require corrections to account for differences in SRF that have not been investigated.

Our study is aimed to fill this gap and to provide quantitative estimates for the effect of SRF among all AVHRR missions. Differences between AVHRR and MODIS, Global Imager (GLI), and Vegetation sensors (VGT) are also considered. To achieve this goal, some representative surface spectral reflectance curves were selected from two observation sources. The first is a database of spectral observation made by the PROBE-1 instrument (Secker, Staenz, Budkewitsch, & Neville, 1999) at the Canada Centre for Remote Sensing (CCRS). The second one is the Advanced Spaceborne Thermal Emission

and Reflection Radiometer (ASTER) spectral library (available from http://speclib.jpl.nasa.gov). The details of the databases are given below. The 6S radiative transfer code (Vermote, Tanré, Deuzé, Herman, & Morcette, 1997) was employed for model simulation of the signal at the top of the atmosphere (TOA) level under various atmospheric conditions and observational geometries.

The paper is organized as follows. Section 2 describes the special features of instrument SRFs. Section 3 discusses the surface spectral library and modeling of satellite signal at the TOA level. Section 4 presents results and an analysis of comparisons between various sensors. Validation results of the model simulation using real satellite observations are shown in Section 5. Section 6 summarizes the research.

2. Sensor SRFs

The SRFs for AVHRR NOAA-6–16, MODIS, GLI, and VGT compatible channels in visible and NIR are shown in Fig. 1a–c. The three panels of Fig. 1 present SRFs for different types of AVHRR: AVHRR/1 (a), installed on morning satellites, AVHRR/2 (b), which was operational on afternoon satellites, and a morning satellite NOAA-12. The bottom panel (c) shows SRFs for AVHRR/3 (NOAA-15 and -16), MODIS, GLI, and VGT. A typical spectrum of green vegetation is also plotted for reference. Though similar, these curves differ in shape, the central wavelength location, the bandwidth, and the degree of overlap between channels, especially with respect to the transition from chlorophyll absorption band to foliage reflection band (0.68–0.72 μm).

Noticeable differences are seen among various AVHRRs. The most notable differences exist between AVHRR/3 on NOAA-15 and -16 and other AVHRRs (Fig. 1b and c). The channels of the new AVHRR/3 have narrower bandwidths and a much smaller overlap over the vegetation transition band. All these factors affect the magnitude of spectral reflectance observed by the sensors and lead to higher NDVI values over vegetated surfaces.

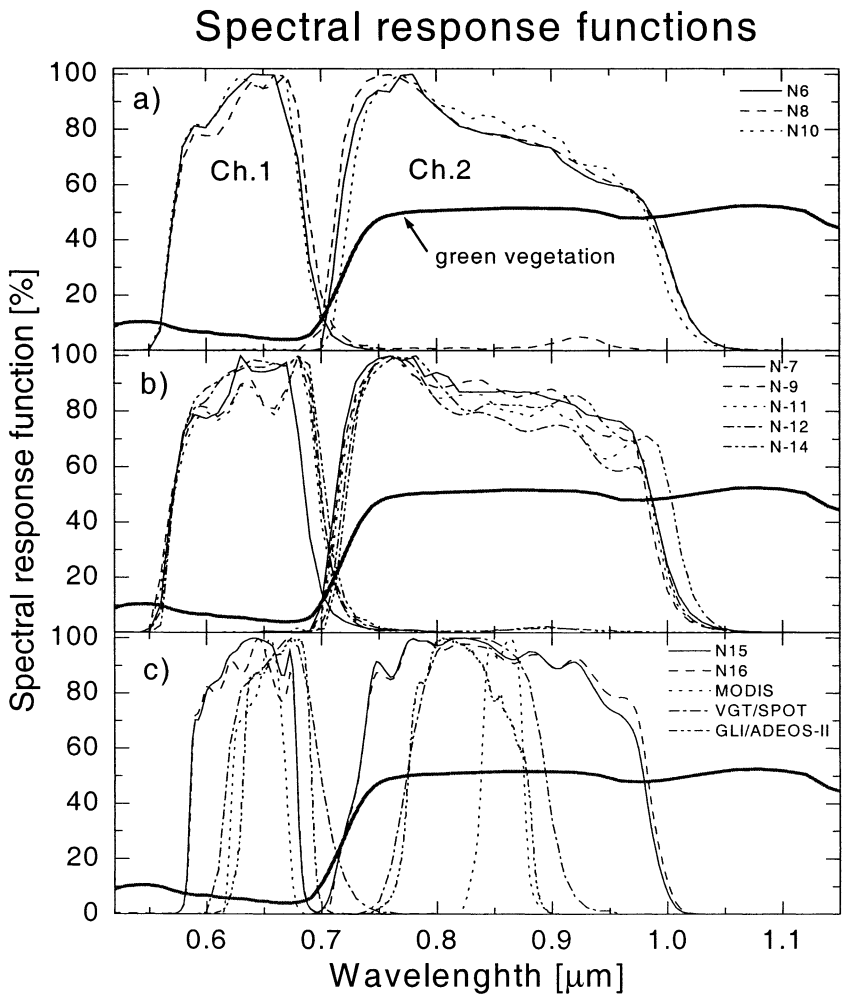

Fig. 1. SRFs of visible (red) and NIR channels for AVHRR NOAA-6–16 and MODIS, VGT, and GLI. (a) AVHRR/1. Morning satellites NOAA-6, -8 and -10. (b) AVHRR/2. Afternoon satellites NOAA-7, -9, -11, and 14 and morning satellite NOAA-12. (c) AVHRR/3 (NOAA-15 and -16), VGT/SPOT, and GLI/ADEOS-II. Typical spectral reflectance curve for green vegetation is shown on each panel.

The MODIS channels are also quite distinct from the AVHRR ones (Fig. 1c). They are much narrower and have no overlap with each other over the vegetation transition band. The MODIS channel 1 is also shifted further to NIR region relative to the AVHRR channel 1. The GLI red channel is close to MODIS, although it is shifted more toward the NIR. The width of the GLI NIR channel is between those for AVHRR and MODIS. The VGT red channel extends beyond 0.7-μm limit, thus causing significant impact on the red reflectances and NDVI. Fig. 1 indicates that a direct comparison of spectral reflectance or vegetation indices produced by various sensors should be made with caution.

3. Surface spectral data and modeling

To encompass a potential range of variability in surface reflectance and NDVI, a set of representative spectra for various surface targets were compiled, following the classification scheme used in the NASA Surface and Atmospheric Radiation Budget (SARB) Project (Rutan & Charlock, 1997). The complete scheme for the SARB Project included 20 different surface classes. Since we had no measurements for some of the surface types and yet the particular focus of this study is on the boreal ecosystem, 12 classes were adopted in this investigation (Fig. 2 and Table 1).

Table 1
Surface types assumed in this study

Surface types
1. Coniferous forest[(1,2)]
2. Deciduous broadleaf forest[(1,2)]
3. Closed shrubland
4. Open shrubland
5. Drygrass/savannah
6. Grassland[(1−4)]
7. Cropland
8. Crop/natural vegetation mosaic
9. Barren/desert
10. Water bodies
11. Fresh snow
12. Coarse granular snow

Superscripts in denote the number of spectral curves used in simulations (Fig. 2).

Surface classes of lower class number nevertheless covered the bulk of variability in spectral reflectance

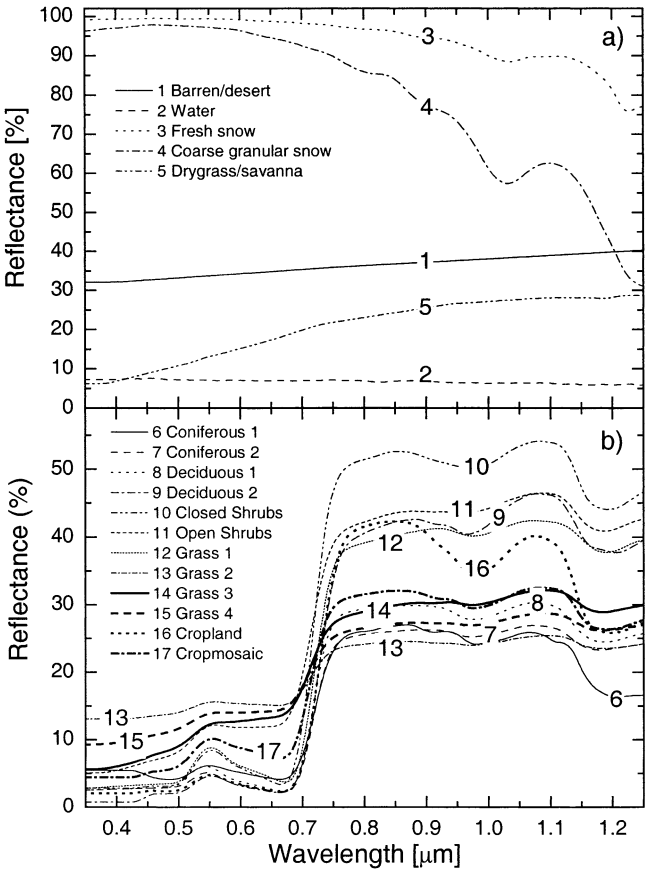

Fig. 2. Spectra of the surface targets used in simulations. They were normalized according to Eq. (1). Top panel (a) shows spectra of nonvegetated surfaces and bottom panel (b) shows spectra for vegetated surfaces.

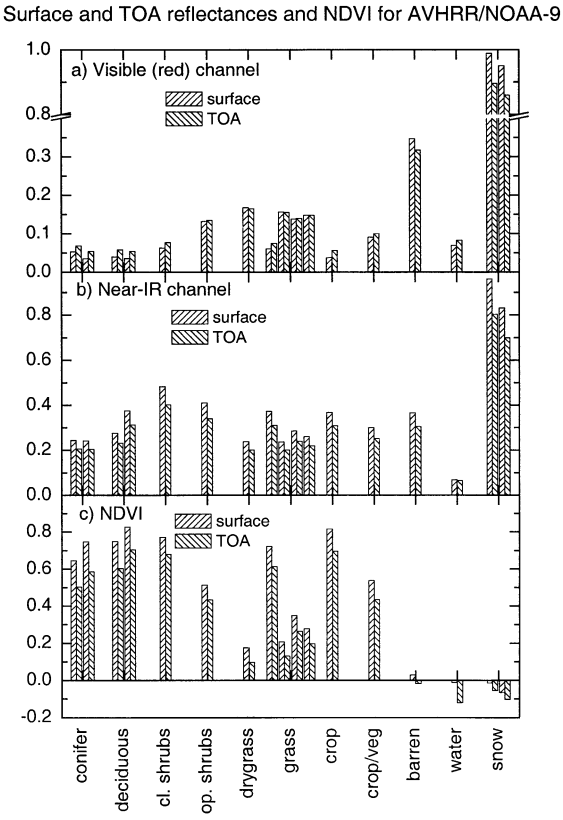

Fig. 3. Surface and TOA reflectances and NDVI for the AVHRR/NOAA-9 for selected spectra. AVHRR onboard the NOAA-9 satellite is considered as the reference sensor following to ISCCP approach (Rossow & Schiffer, 1999). Visible (red), NIR reflectances, and NDVI are presented in sequence from top to bottom. Note the break in vertical scale between 0.4 and 0.8 for the visible channel.

occurred in nature. Classes 1 and 2 are depicted by two spectral curves each, and class 6 (grassland) is described by four curves with different values of NDVI to reflect various vegetation density levels.

Spectral curves were derived from two sources: aircraft observations from the PROBE-1 instrument made by the Canada Centre for Remote Sensing (Secker et al., 1999). The PROBE-1 is airborne hyperspectral sensor covering visible and NIR spectral regions with 128 spectral bands. The second source was acquired from the ASTER spectral library. We normalized each spectrum to reproduce SARB broadband albedo, i.e.,

$$\tilde{\rho}(\lambda) = \alpha_{\mathrm{SARB}} \frac{\int_{\lambda\min}^{\lambda\max} S_0(\lambda)\mathrm{d}\lambda}{\int_{\lambda\min}^{\lambda\max} S_0(\lambda)\rho(\lambda)\mathrm{d}\lambda}, \quad (1)$$

where $S_0(\lambda)$ and $\rho(\lambda)$ are the solar spectral constant and observed spectral reflectance, and α_{SARB} is the broadband albedo from Rutan and Charlock (1997). The normalization (Eq. (1)) provides a link of individual spectral curves to a specific SARB surface type. The derived spectra (Fig. 2) are shown for the wavelength interval 0.35–1.25 μm, which essentially covers visible and NIR portion of the solar

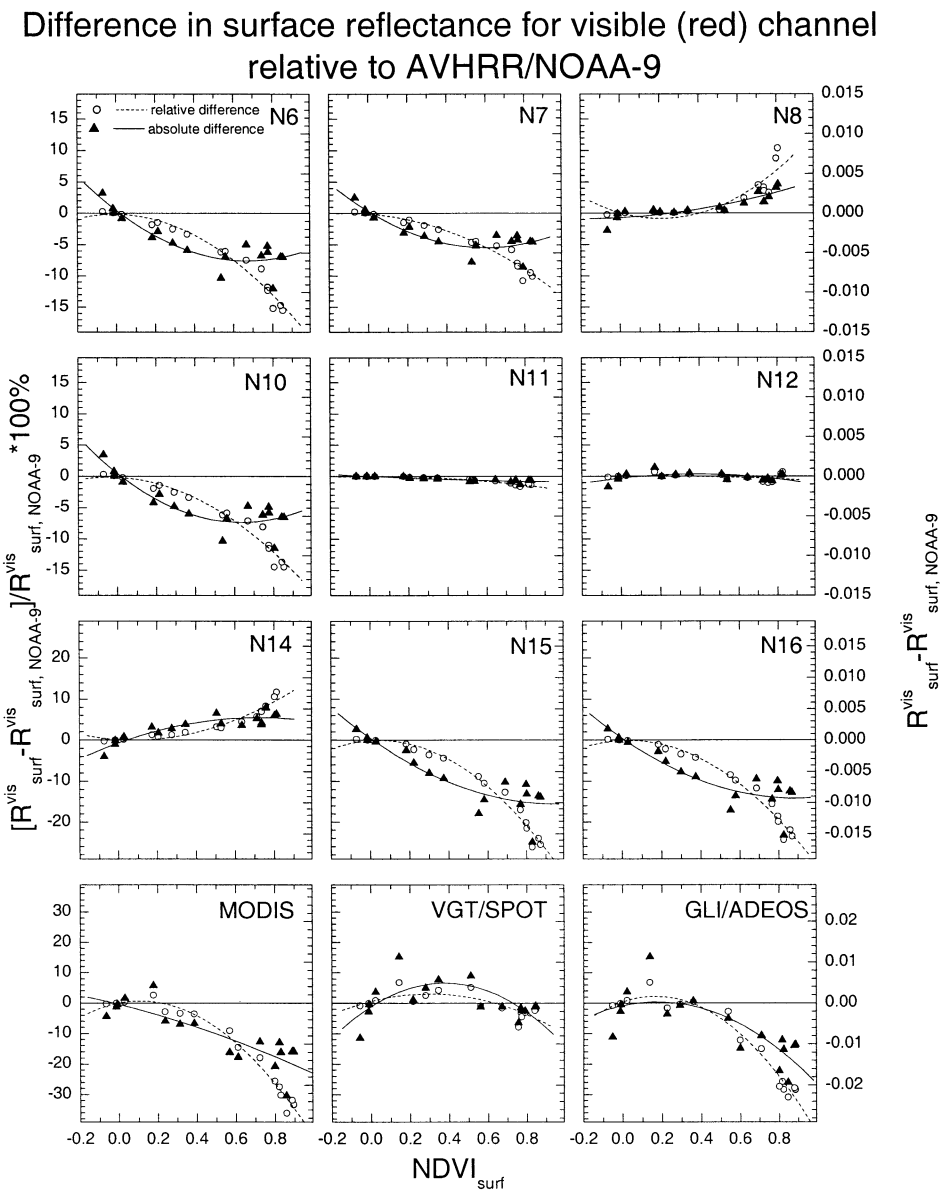

Fig. 4. Absolute (solid triangles) and relative (open circles) differences in visible (red) channel reflectances at the surface level with respect to AVHRR/NOAA-9. The left scale is for relative difference and the right scale is for absolute difference. All data points are plotted versus NDVI of particular sensor. Quadratic best fits for absolute (solid) and relative (dashed) differences are also shown. Parameters of fitting curves are given in Table 2.

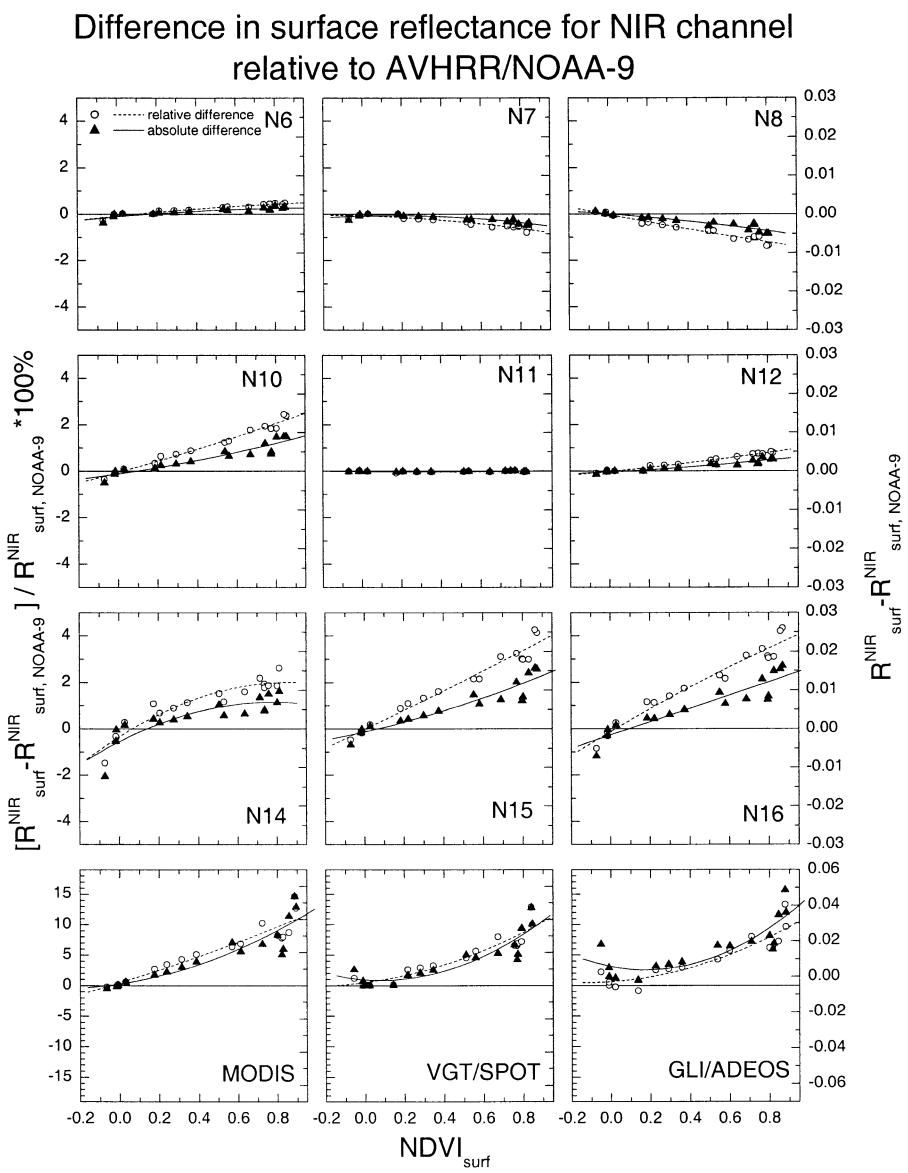

Fig. 5. Similar to Fig. 4, but for the NIR channel at the surface level. Parameters of fitting curves are given in Table 3.

spectrum under study. The top panel (Fig. 2a) depicts spectra of nonvegetated surfaces and a dry grass/savannah surface, and the bottom panel (Fig. 2b) shows spectra for various vegetated surfaces. The steep increase in reflectivity above 0.7 μm is a characteristic feature of these curves. The data selected encompass spectral differences between various natural surface classes.

4. Modeling results

4.1. Radiative transfer modeling

The 6S radiative transfer model was employed to simulate the TOA signal. The wavelength increment of the model is 2.5 nm, which allows us to accurately resolve all spectral features of the targets and instrument SRF. Baseline simulations were conducted for US62 atmospheric profile with total water vapor (TWV) columnar amount scaled to 1.5 cm, representative for the boreal region in summer time (Cihlar, Tcherednichenko, Latifovic, Li, & Chen, 2000). The ozone content was set to 350 Dobson units (DU). Since satellite studies of surface properties usually employ clear-sky composites selected for the highest atmospheric transparency, the AOD was set to 0.06, as recommended by Fedosejevs et al. (2000) for the Canadian boreal zone. The surface reflectance was assumed to be Lambertian, i.e., independent of sun-sensor geometry. The TOA reflectance has a certain dependence on observational geometry due to atmospheric effects. We conducted computations for various geometrical conditions: the SZA θ_0 varying from 0° to 75° with 15° steps, the viewing zenith angle (VZA) θ from 0° to 45° with 15° steps, and the relative azimuth angle (RAA) ϕ was set to 0°, 90°, and

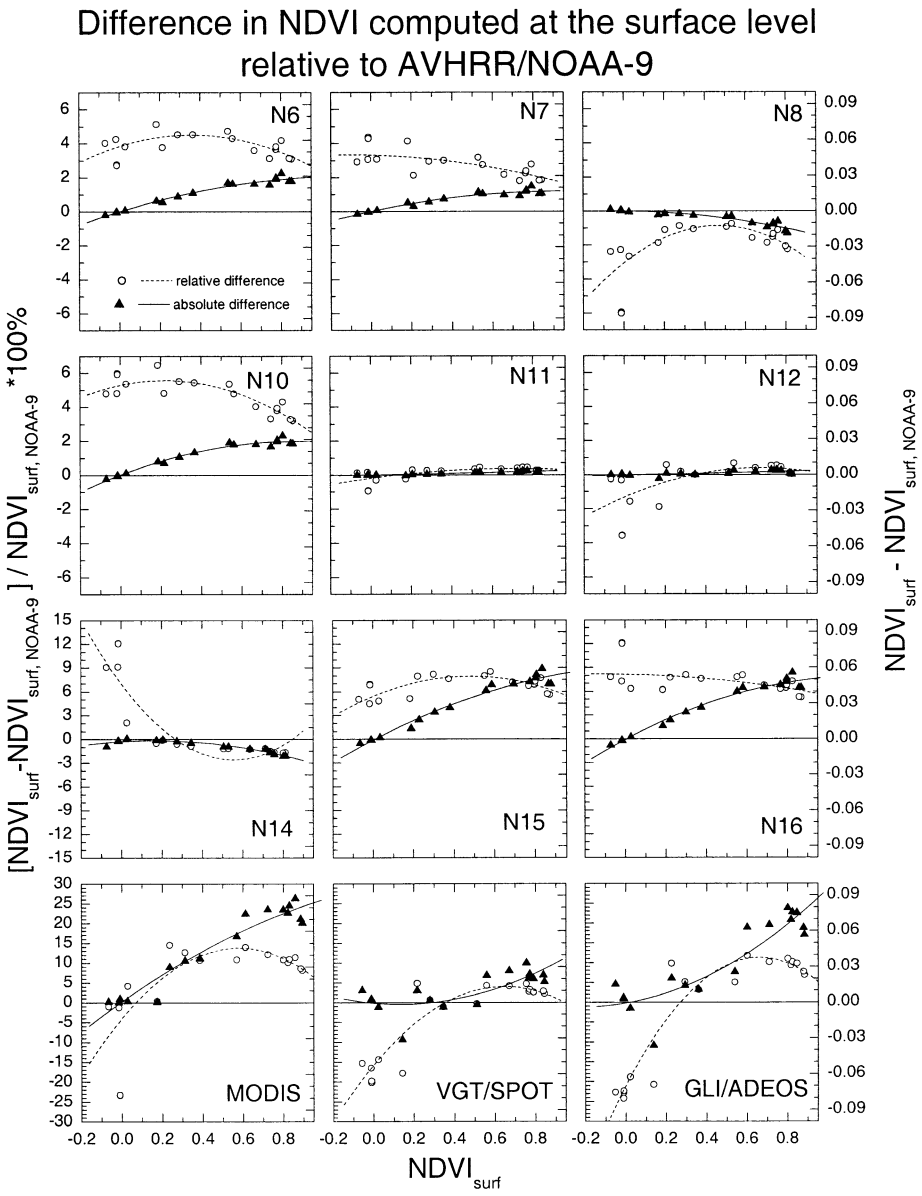

Fig. 6. Similar to Figs. 4 and 5, but for NDVI at the surface level. Parameters of fitting curves are given in Table 4.

Table 2
Parameters of quadratic best fit to absolute spectral correction $\Delta\rho = \rho - \rho_{NOAA\text{-}9}$ and relative spectral correction $\Delta\rho = (\rho - \rho_{NOAA\text{-}9})/(\rho_{NOAA\text{-}9})$ (%) for visible (red) channel

Instrument	Absolute correction	r^2	σ	Relative correction (%)	r^2	σ (%)
AVHRR/N-6	$0.00035 - 0.0189X + 0.0141X^2$	.80	0.0013	$-0.160 - 0.445X - 19.525X^2$	.97	0.97
AVHRR/N-7	$0.00026 - 0.0153X + 0.0127X^2$	.77	0.0010	$0.108 - 2.230X - 11.050X^2$	.96	0.76
AVHRR/N-8	$-0.00056 + 0.0014X + 0.0033X^2$	.77	0.0007	$0.087 - 9.037X + 21.721X^2$	.81	1.37
AVHRR/N-10	$0.00037 - 0.0195X + 0.0153X^2$	.79	0.0014	$-0.159 - 1.411X - 16.949X^2$	.96	1.0
AVHRR/N-11	$0.00001 - 0.0012X + 0.0005X^2$	.76	0.0002	$0.006 + 0.0744X - 2.335X^2$	.96	0.12
AVHRR/N-12	$-0.00022 + 0.0027X - 0.0035X^2$	.21	0.0005	$0.073 + 0.1604X - 0.947X^2$	.14	0.47
AVHRR/N-14	$-0.00046 + 0.0112X - 0.0077X^2$	.82	0.0008	$0.116 - 2.951X + 18.076X^2$	.94	0.87
AVHRR/N-15	$0.00029 - 0.0222X + 0.0117X^2$	.81	0.0021	$-0.105 + 3.115X - 36.306X^2$	.98	1.31
AVHRR/N-16	$0.00028 - 0.0217X + 0.0123X^2$	.80	0.0020	$-0.096 + 2.044X - 32.746X^2$	.98	1.26
MODIS	$-0.00037 - 0.0118X - 0.0051X^2$	.73	0.0035	$0.046 + 12.136X - 56.504X^2$	.98	1.87
VGT/SPOT	$-0.00086 + 0.0305X - 0.0404X^2$	.42	0.0034	$0.570 + 16.234X - 27.183X^2$	.58	2.29
GLI/ADEOS	$-0.00063 + 0.0103X - 0.0297X^2$	.62	0.0045	$0.419 + 21.432X - 65.063X^2$	.96	2.51

Surface level. X denotes NDVI for particular sensor computed at the surface level.

Table 3
Similar to Table 2, but for NIR channel

Instrument	Absolute correction	r^2	σ	Relative correction (%)	r^2	σ (%)
AVHRR/N-6	$-0.00069+0.00443X-0.0021X^2$	.79	0.0005	$-0.0777+0.8707X-0.2788X^2$	.95	0.05
AVHRR/N-7	$-0.00049+0.00142X-0.0045X^2$	.77	0.0004	$-0.0682-0.2536X-0.5465X^2$	.90	0.08
AVHRR/N-8	$0.00005-0.00385X-0.002X^2$	.88	0.0006	$-0.0205-1.5927X+0.1487X^2$	.96	0.10
AVHRR/N-10	$-0.00073+0.00745X+0.0031X^2$	.89	0.0012	$-0.0539+2.3498X+0.3563X^2$	.98	0.13
AVHRR/N-11	$-0.00008-0.0001X+0.0002X^2$	.11	0.0001	$-0.0140-0.1087X+0.1505X^2$	.19	0.02
AVHRR/N-12	$-0.00025+0.00264X+0.0014X^2$	.90	0.0004	$-0.0184+0.8199X+0.2289X^2$	.98	0.04
AVHRR/N-14	$-0.00335+0.02615X-0.0168X^2$	.74	0.0026	$-0.3457+5.4112X-3.1057X^2$	.89	0.33
AVHRR/N-15	$-0.00082+0.01153X+0.0051X^2$	.88	0.0020	$-0.03087+4.0655X+0.210X^2$	.96	0.29
AVHRR/N-16	$-0.00164+0.01696X+0.0002X^2$	.86	0.0023	$-0.12313+5.0171X-0.669X^2$	.96	0.32
MODIS	$0.00101+0.01788X+0.028X^2$	.82	0.0069	$0.4773+9.8974X+1.9483X^2$	.89	1.46
VGT/SPOT	$0.00349-0.00826X+0.0532X^2$	.81	0.0059	$0.4960+4.1976X+7.6205X^2$	.88	1.25
GLI/ADEOS	$0.0056-0.021X+0.0605X^2$	.73	0.0070	$0.6173+2.1544X+8.6714X^2$	.83	1.52

Surface level. X denotes NDVI for particular sensor computed at the surface level.

180°. For sensitivity tests, the following values were chosen: 0, 0.06, and 0.6 for AOD; 0.5, 1.5, and 5.0 cm for TWV; 270, 350, and 430 DU for ozone. The simulations were done for a viewing geometry at $\theta_0=45°$, $\theta=0°$, and $\phi=0°$, a typical geometry for normalizing satellite observations (Trishchenko et al., in press).

The range of variability in reflectance and NDVI values simulated for the AVHRR on board NOAA-9 over all surface targets is illustrated in Fig. 3. This radiometer is often considered as a reference instrument (e.g., Rossow & Schiffer, 1999). Note the break in vertical scale for visible channel in Fig. 3a, which was introduced to show enough details for low reflective surfaces as well as the highly reflective snow surface. The reflectance in visible (red) band for vegetated surfaces ranges from 0.05 to 0.15. At the surface, the values are typically smaller because scattering by atmospheric molecules adds to the signal reflected from darker surfaces. The opposite is true for the NIR band where surface reflectance is higher than at the TOA, because atmospheric attenuation outweighs scattering back to the sensor. These relationships also explain why NDVI at the TOA level is typically smaller than at the surface level. The NDVI is either very small or even negative for nonvegetated surfaces, such as water, snow, and barren/desert classes.

4.2. Surface level

Figs. 4–6 show the surface level results for visible (red), NIR reflectances, and NDVI. The absolute and relative differences with respect to AVHRR/NOAA-9 values are plotted against NDVI for each sensor. The difference is also referred to as the spectral correction factor. The least differences are found for AVHRR/NOAA-11 followed by NOAA-12. Other AVHRR/1,2 are reasonably close to AVHRR/NOAA-9, although the differences could reach 0.01 (10–15% relative) for red channel (Fig. 4), 0.01 (2–3%) for NIR channel (Fig. 5), and 0.03 (4–6%) for NDVI of vegetated surfaces (Fig. 6). Since NDVI for sparse vegetation and nonvegetated targets are small, the relative differences in NDVI for these surface types are larger.

The sensor spectral reflectances and NDVI differ systematically for AVHRR/3 onboard the NOAA-15 and -16. The visible (red) reflectance for AVHRR/3 is smaller by 0.01–0.015 (20–25%; Fig. 4), while the NIR channel reflectance is larger by 0.01–0.015 (3–4%; Fig. 5). As a

Table 4
Similar to Tables 2 and 3, but for NDVI

Instrument	Absolute correction	r^2	σ	Relative correction (%)	r^2	σ (%)
AVHRR/N-6	$0.00005+0.052X-0.02278X^2$	.97	0.0021	$3.84+3.7437X-5.227X^2$	.43	0.48
AVHRR/N-7	$0.00001+0.03632X-0.0196X^2$	.93	0.0018	$3.315-0.3486X-1.459X^2$	.50	0.50
AVHRR/N-8	$0.00006-0.0018X-0.0205X^2$	.88	0.0021	$-3.0562+9.4069X-10.072X^2$	.50	0.84
AVHRR/N-10	$0.0002+0.0648X-0.0372X^2$	.97	0.0020	$5.301+2.526X-5.774X^2$	.77	0.45
AVHRR/N-11	$-0.0001+0.0031X+0.00072X^2$	.87	0.0005	$-0.1952+1.601X-1.137X^2$	.47	0.25
AVHRR/N-12	$-0.00032+0.0031X+0.0007X^2$	.39	0.0015	$-1.316+5.1X-3.795X^2$	.44	0.82
AVHRR/N-14	$-0.00201+0.0099X-0.0304X^2$	.93	0.0013	$6.986-34.3909X+30.8637X^2$	.83	1.81
AVHRR/N-15	$-0.00026+0.0877X-0.0307X^2$	.97	0.0038	$5.4+10.478X-10.894X^2$	.57	0.82
AVHRR/N-16	$-0.00061+0.091X-0.0391X^2$	.97	0.0034	$8.139-0.4926X-2.1904\ X^2$	.29	1.25
MODIS	$0.00068+0.1199X-0.03383X^2$	.94	0.0084	$-3.993+61.4265X-53.129X^2$	.59	5.70
VGT/SPOT	$-0.0006-0.0153X+0.05836X^2$	.54	0.0104	$-15.758+61.013X-47.087X^2$	.82	3.77
GLI/ADEOS	$-0.00086+0.0295X+0.0667X^2$	.81	0.0149	$-20.982+97.84X-74.127X^2$	.89	4.62

Surface level.

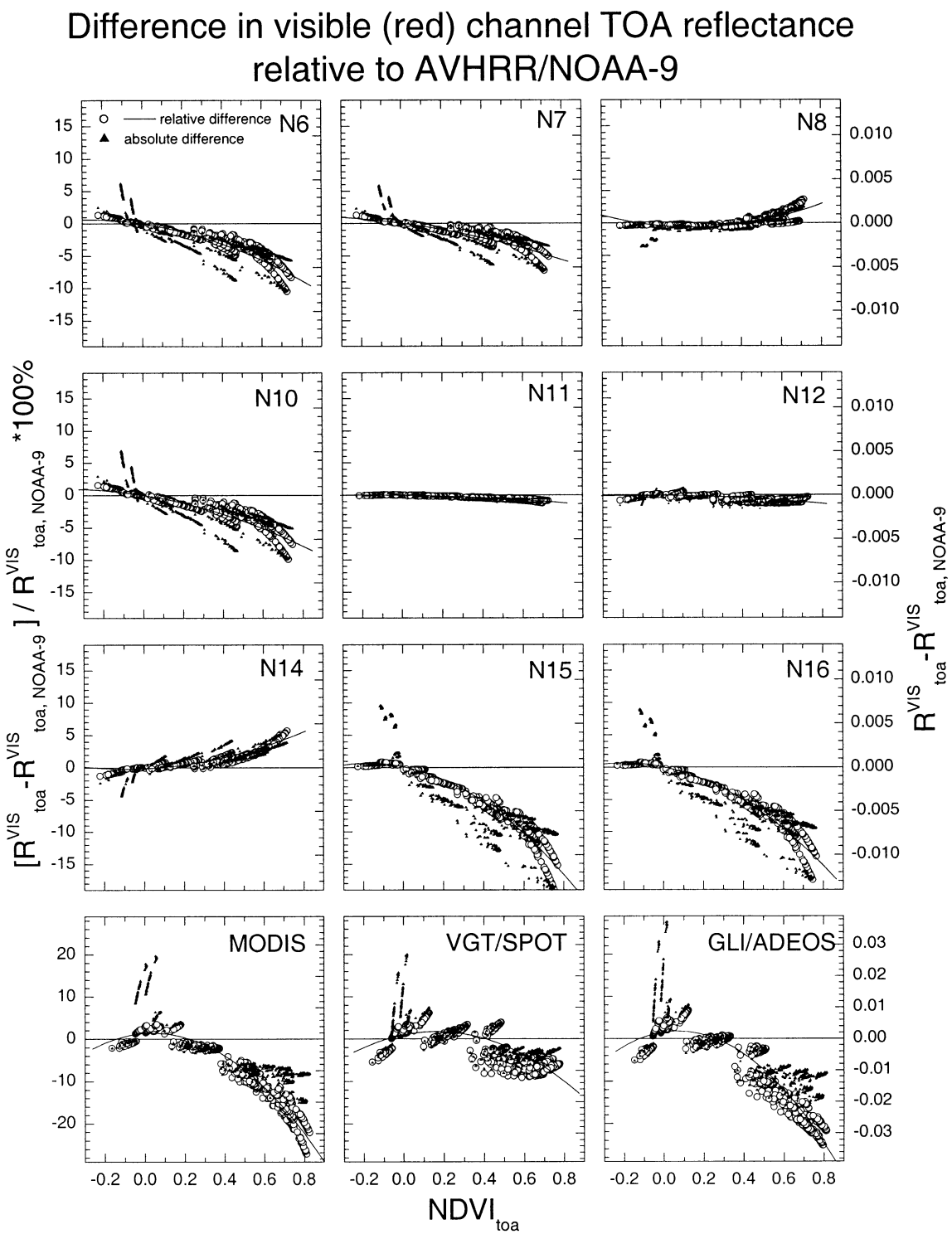

Fig. 7. Absolute (solid triangles) and relative (open circles) differences in visible (red) channel reflectances at the TOA levels with respect to AVHRR/NOAA-9. Solid lines correspond to quadratic fit to relative difference. Parameters of fitting curves are given in Table 5.

result, NDVI derived from AVHRR/NOAA-15 or -16 is higher by 0.03–0.06 (5–10%; Fig. 6). These differences are due to (1) a significantly narrower spectral band of the visible (red) channel that is much less contaminated by the elevated reflection in NIR and (2) the NIR channel that is less influenced by the transition band (Fig. 1c).

The SRFs of MODIS and GLI are so different from that of AVHRR/NOAA-9 that the surface reflectance differences reaches 0.02 (20–30%) in visible channel (Fig. 4), 0.04–0.05 (10–15%) in NIR channel (Fig. 5), and 0.06–0.09 (20–25%) in NDVI (Fig. 6). The SRF effect for VGT is smaller than for MODIS and GLI and comparable to AVHRR/3. The

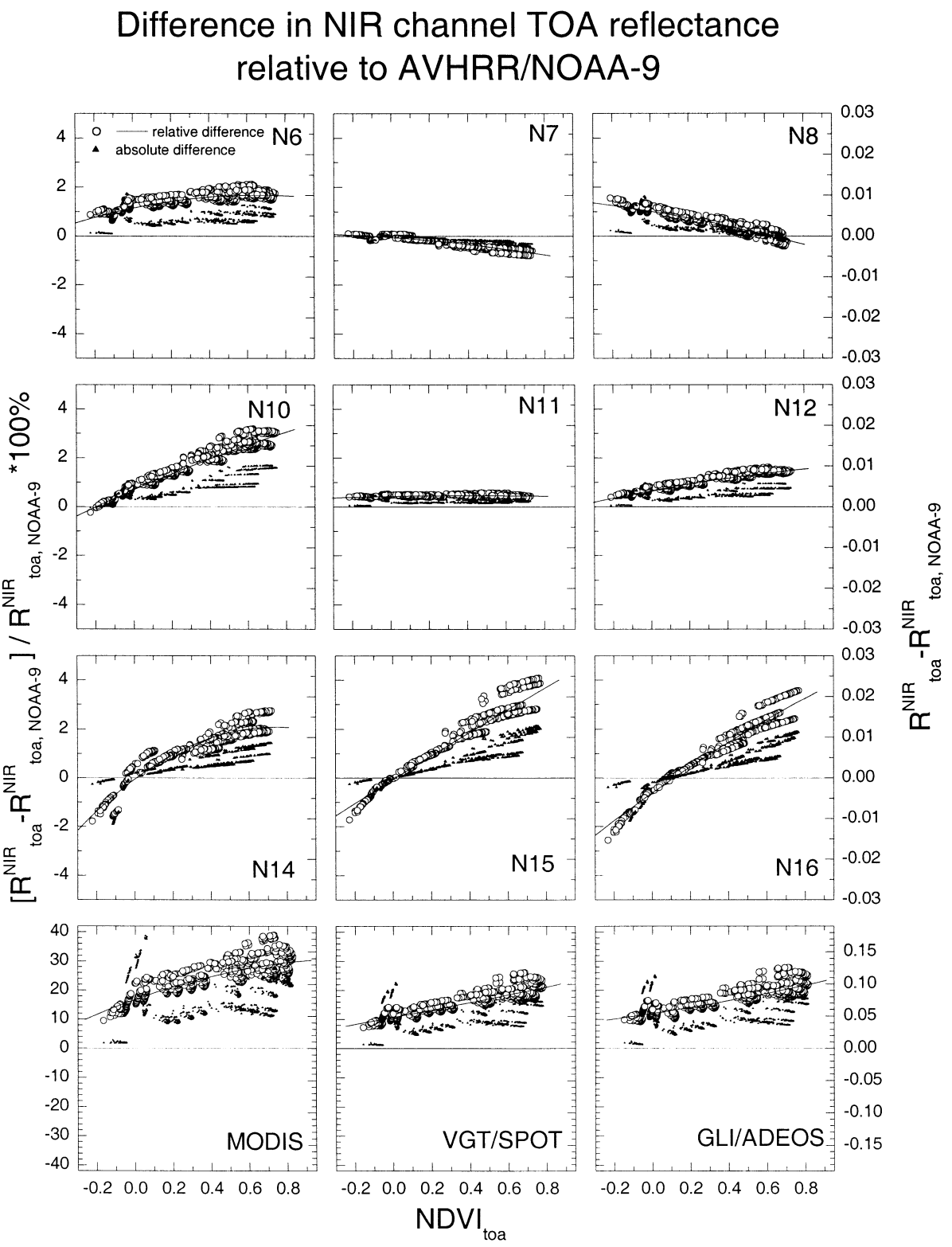

Fig. 8. Similar to Fig. 7, but for NIR channel reflectances at the TOA level. Parameters of fitting curves are given in Table 6.

difference could be as large as 0.01 ($\sim$10%) in the visible (red) channel, 0.02–0.04 (5–10%) in the NIR channel, and 0.03 ($\sim$5–10%) in NDVI for vegetated surfaces.

The discrepancies caused by different SRFs may be corrected using the second degree polynomial functions, as shown in Figs. 4–6. The curves were produced by fitting

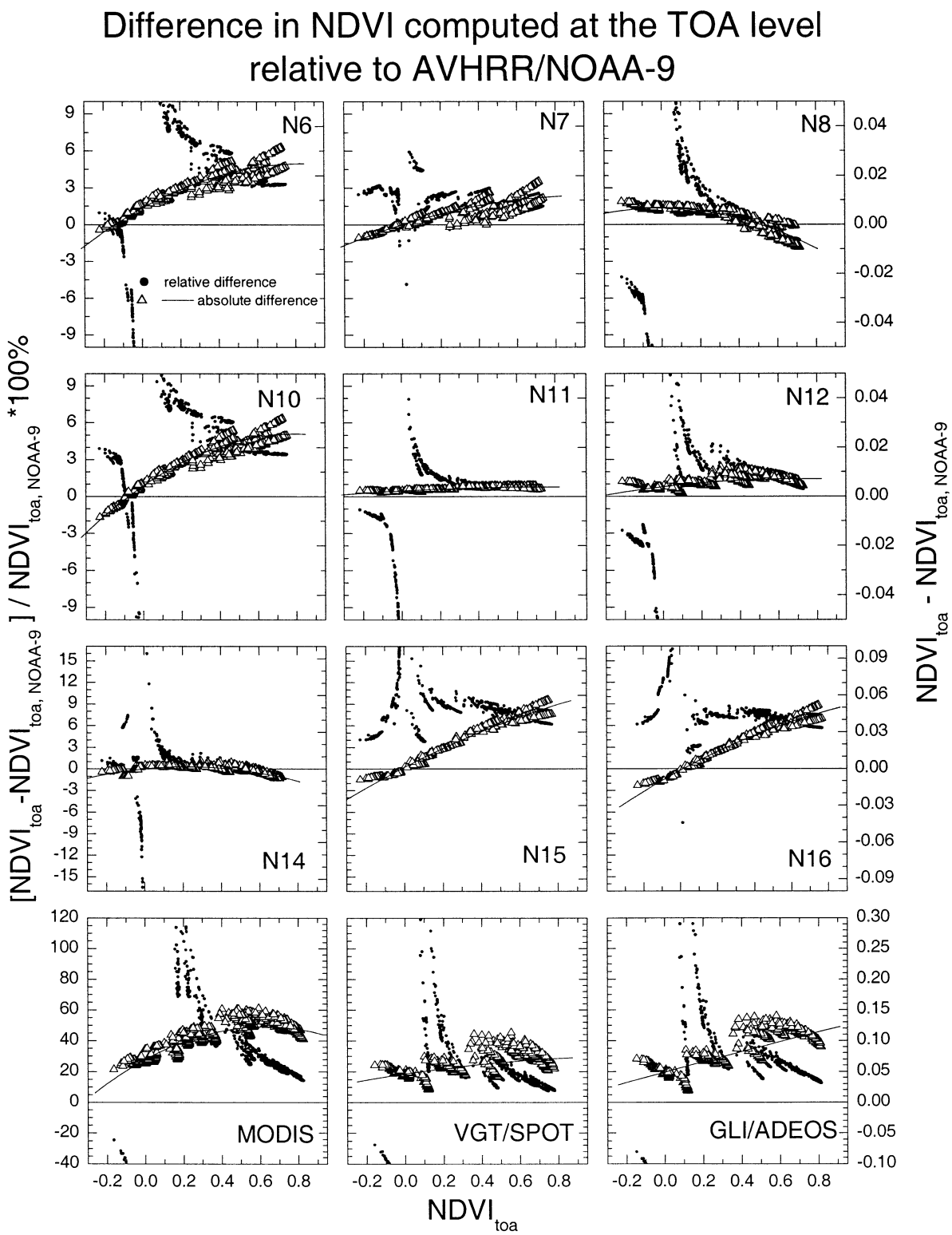

Fig. 9. Similar to Figs. 7 and 8, but for NDVI at the TOA level. Quadratic fit is plotted for absolute difference in NDVI due to SRF effect. Parameters of fitting curves are given in Table 7.

the data points. Tables 2–4 give the coefficients of the quadratic functions that best fit the data, correlation coefficient, and standard deviation of the fit for each sensor for visible, NIR, and NDVI, respectively. The quality of the fits is quite good for AVHRRs and MODIS, while data for VGT and GLI sensors are more scattered.

Table 5
Parameters of polynomial fit to the relative spectral correction $\Delta\rho = (\rho - \rho_{NOAA\text{-}9})/(\rho_{NOAA\text{-}9})$ (%) for visible (red) channel

Instrument	Relative correction (%)	r^2	σ (%)
AVHRR/N-6	$-0.01588-4.62556X-7.96852X^2$	.93	0.77
AVHRR/N-7	$0.04201-4.12357X-3.67224X^2$	.88	0.68
AVHRR/N-8	$-0.41911-2.87354X+8.89133X^2$	.65	0.60
AVHRR/N-10	$0.01277-4.84277X-6.23082X^2$	.90	0.84
AVHRR/N-11	$-0.01258-0.48667X-1.27999X^2$	.94	0.09
AVHRR/N-12	$-0.09189-0.2534X-1.66716X^2$	.53	0.35
AVHRR/N-14	$-0.15411+1.30802X+7.27126X^2$	.92	0.47
AVHRR/N-15	$0.10932-6.31443X-18.25781X^2$	.97	0.98
AVHRR/N-16	$0.04244-6.30091X-16.02976X^2$	.96	0.96
MODIS	$1.37765+3.11606X-40.78357X^2$	.96	1.71
VGT/SPOT	$1.01934+9.33224X-28.91508X^2$	.70	2.38
GLI/ADEOS	$1.5794+6.87468X-49.41134X^2$	.93	2.60

TOA level. X denotes NDVI for particular sensor computed at the TOA level.

4.3. TOA level

The general trends of the effect of SRF at the TOA are similar to those at the surface but differ in detailed features as a result of the distortion by the atmosphere. Discrepancies in TOA visible, NIR reflectance, and NDVI with respect to AVHRR/NOAA-9 are shown in Figs. 7–9. Quadratic fits to the relative differences in reflectances and absolute difference in NDVI are also plotted. Other data points are more scattered and no fits are presented. For example, the relative difference for NDVI may be extremely large for some combinations, simply because NDVI values computed at the TOA level are very close to zero. Figs. 7–9 contain more points than figures for the surface level because of the variable effects of the atmosphere and observation geometry. Therefore, fitting all data points with one curve is just a bulk approximation of the SRF effect to account for the large SRF effect (e.g., MODIS, VGT, and GLI). In the case of AVHRR sensors, the approach still provides a good approximation of the effect of SRF. The parameters of fitting curves are given in Tables 5–7.

Table 6
Similar to Table 4, but for NIR channel reflectance at the TOA level

Instrument	Relative correction (%)	r^2	σ (%)
AVHRR/N-6	$1.13467+1.64781X-1.26708X^2$	.72	0.17
AVHRR/N-7	$-0.05851-0.53685X-0.44445X^2$	.89	0.08
AVHRR/N-8	$1.00893-1.28713X-0.49973X^2$	.90	0.14
AVHRR/N-10	$0.67763+3.41197X-0.56705X^2$	.95	0.21
AVHRR/N-11	$0.41666+0.15057X-0.16803X^2$	.14	0.04
AVHRR/N-12	$0.65109+1.4419X-0.42437X^2$	.92	0.10
AVHRR/N-14	$-0.06817+5.81785X-3.93554X^2$	.89	0.36
AVHRR/N-15	$-0.07092+4.90503X-0.23422X^2$	.96	0.30
AVHRR/N-16	$-0.62499+5.51994X-0.84905X^2$	.96	0.30
MODIS	$16.69042+23.8168X-9.82829X^2$	.72	3.10
VGT/SPOT	$10.65846+12.30469X+0.97572X^2$	.80	1.88
GLI/ADEOS	$11.94219+9.91694X+2.78224X^2$	.75	2.14

X denotes NDVI for particular sensor computed at the TOA level.

Table 7
Parameters of polynomial fit to the absolute spectral correction for NDVI

Instrument	Absolute correction (%)	r^2	σ (%)
AVHRR/N-6	$0.00659+0.0435X-0.02586X^2$	.93	0.0023
AVHRR/N-7	$-0+0.02435X-0.0125X^2$	.82	0.0023
AVHRR/N-8	$0.00668-0.00023X-0.02523X^2$	.84	0.0019
AVHRR/N-10	$0.00431+0.05377X-0.03415X^2$	.95	0.0022
AVHRR/N-11	$0.00224+0.00428X-0.00276X^2$	.77	0.0004
AVHRR/N-12	$0.00383+0.00911X-0.00633X^2$	.46	0.0017
AVHRR/N-14	$0.00003+0.01558X-0.03521X^2$	.66	0.0018
AVHRR/N-15	$0.00112+0.08104X-0.02105X^2$	.98	0.0032
AVHRR/N-16	$-0.00138+0.08156X-0.02569X^2$	.98	0.0028
MODIS	$0.06948+0.16993X-0.13581X^2$	.82	0.0105
VGT/SPOT	$0.04608+0.04565X-0.01774X^2$	.35	0.0134
GLI/ADEOS	$0.04879+0.08439X-0.0035X^2$	.71	0.0160

TOA level. X denotes NDVI for particular sensor computed at the TOA level.

Similar to the surface case, the best agreement with AVHRR/NOAA-9 was found for AVHRR/NOAA-11. For all remaining AVHRRs, the atmospheric effect generally diminishes the spectral difference for the visible (red) channel and slightly increases it in the NIR. The absolute discrepancies in NDVI remain essentially the same as at the surface, 0.03–0.06 (Fig. 9). The effect on NDVI for NOAA-7, -8, -11, -12, and -14 is typically within ±0.01. For NOAA-6 and -10, the differences in NDVI relative to NOAA-9 were as much as 0.02–0.03 (3–5% for vegetated surfaces). The largest discrepancy was observed for NOAA-15 and -16. The absolute difference in NDVI could be as high as 0.03–0.06, which is larger than 10% for vegetated targets.

The corrections for visible channels of MODIS, VGT, and GLI sensors at the TOA level shown in Fig. 7 are similar in magnitude to those at the surface, but the magnitude of spectral correction for the NIR channels is much higher (Fig. 8). Apart from the same reasons as for surface, the narrow NIR spectral channels are not affected by atmospheric absorption in the 0.94-μm water vapor absorption band. Consequently, the relative differences between these sensors and AVHRR/NOAA-9 were as much as 20–40%, with the largest differences occurred between AVHRR and MODIS (up to 40%). The results for VGT and GLI are similar but smaller than for MODIS. The difference $(\rho_{NIR} - \rho_{NIR,NOAA\text{-}9})$ is positive in all cases and increases with NDVI.

4.4. Sensitivity of spectral correction to atmospheric state

Although the spectral effects discussed above are representative for "nominal" conditions described above, it is also likely that in any particular comparison the magnitude of the differences is affected by the variable atmospheric state. Major variables influencing satellite measurements are AOD, TWV, and ozone columnar amounts. To investigate how variations in the atmospheric state affect the spectral correction factors, a sensitivity factor of spectral

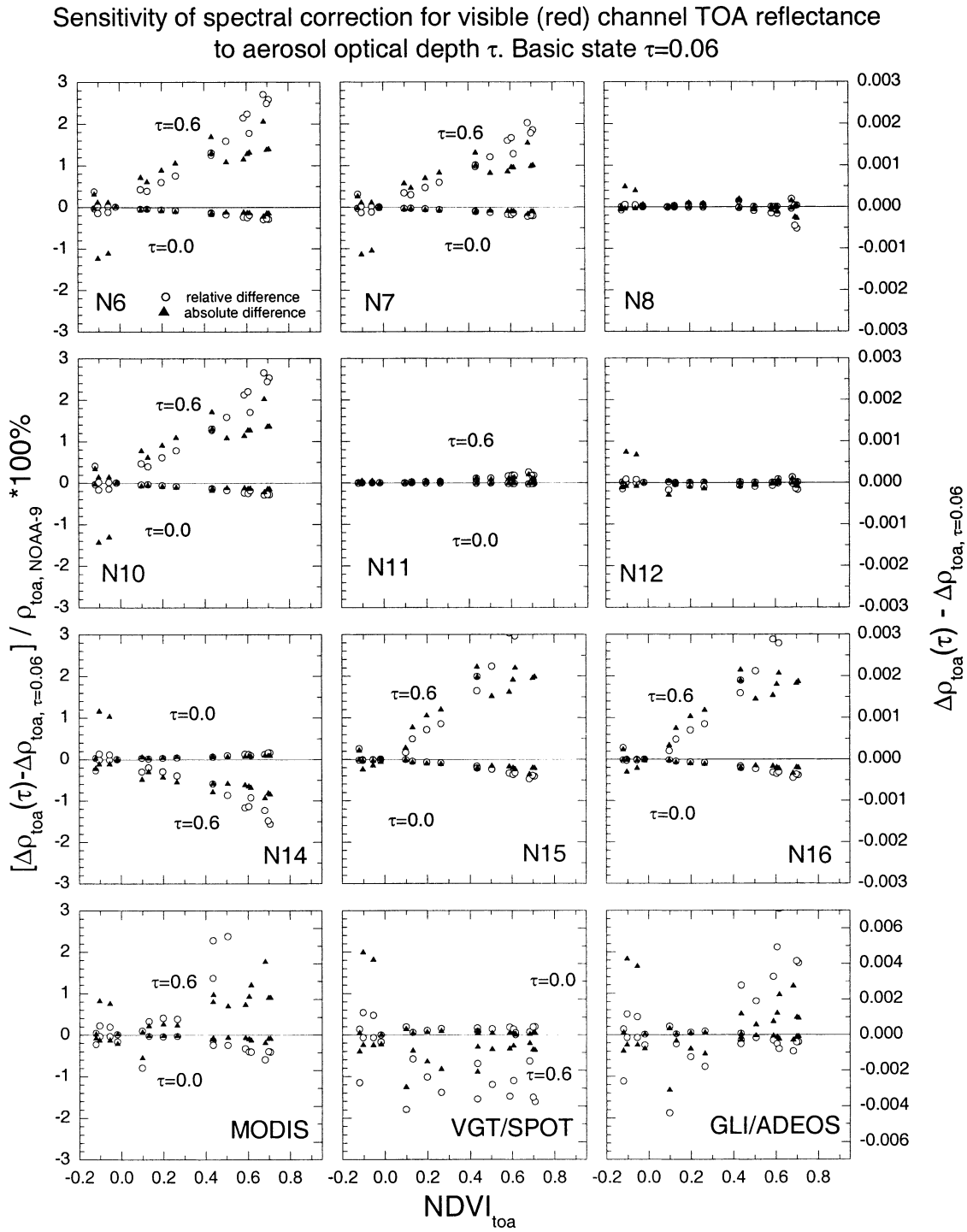

Fig. 10. Sensitivity of SRF effect to AOD τ. Visible (red) channel reflectance at the TOA level. AOD for the basic atmospheric state is 0.06, TWV is 1.5 cm, and ozone content is 350 DU. Computations were done for no aerosol ($\tau = 0$) and hazy ($\tau = 0.6$) cases.

correction $(\Delta\rho)'$ to the atmospheric constituent A is defined as

$$(\Delta\rho)'_i = \Delta\rho_i(A) - \Delta\rho_i(A_0), \quad (2)$$

where

$$\Delta\rho_i(A) = \rho_i(A) - \rho_{\mathrm{AVHRR/NOAA-9}}(A), \quad (3)$$

A is the amount of TWV, ozone, or AOD; A_0 is the corresponding amount for the basic (or reference) atmospheric state; index i refers to a specific satellite sensor; and ρ denotes the reflectance or NDVI. Normalized (relative) sensitivity is computed as the ratio $[(\Delta\rho)'/\rho_{\mathrm{AVHRR/NOAA\text{-}9}}] \times 100\%$ (Eqs. (2) and (3)).

4.4.1. Water vapor amount

The sensitivity tests of spectral effect to the amount of TWV in the atmospheric column are computed for the NIR channels and NDVI (figures not included), since water vapor effect in the visible band is not significant. The tests were conducted for the basic atmospheric state (1.5 cm) and two extreme values, 0.5 cm (dry case) and 5 cm (humid case). The ozone amount was fixed at 350 DU and the AOD at 0.06. The sensitivity of spectral correction to precipitable water vapor is rather small for the AVHRR NIR channels relative to the magnitude of the spectral correction itself. It is well within 1% of AVHRR/NOAA-9 reflectance and typically three to five times smaller than spectral correction computed for the basic atmospheric state. Since water vapor has essentially no effect on visible reflectance, corrections to NDVI are also small. For other sensors (MODIS, VGT, and GLI), the sensitivity to water vapor is somewhat larger. The spectral adjustment for MODIS NIR channel is about -6% and $7-8\%$ for TWV = 0.5 and 5 cm, respectively, relative to the standard case of TWV = 1.5 cm. Corrections for NIR channel reflectance of VGT and GLI sensors are within $\pm 3\%$. For NDVI, absolute corrections range from -0.03 to 0.04 for MODIS and from -0.015 to 0.02 for NDVI of VGT and GLI.

Based on these results, we may conclude that the effect of atmospheric water vapor is negligible when making spectral adjustments among various AVHRRs. This is because the various sensors have similar spectral coverage, in particular with respect to water vapor absorption bands. Note that the spectral correction effect under study should not be confused with the absolute effect of TWV on NIR reflectance itself. The latter is a lot more significant (Cihlar et al., 2000). The situation is more complicated for MODIS, VGT, and GLI sensors. The TOA reflectances measured by these sensors are less sensitive to water vapor, since SRF for these instruments do not include the strong water absorption band around 0.94 μm. Nevertheless, since we estimate the effect of spectral correction relative to AVHRR, which is quite sensitive to water vapor amount (Cihlar et al., 2000), the sensitivity of spectral correction to water vapor emerges for these sensors.

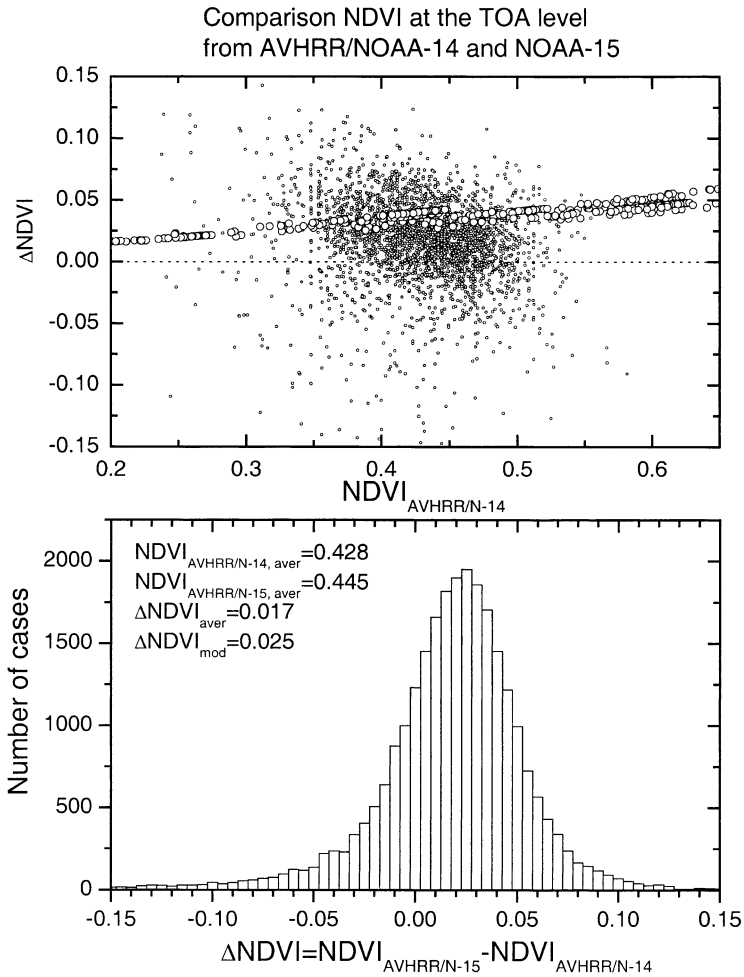

Fig. 11. Top panel shows comparison of NDVI computed at the TOA level from AVHRR/NOAA-14 and -15. Small dots denote satellite observations. Open circles denote model simulations. Bottom panel shows distribution of difference in ΔNVI.

4.4.2. AOD

The sensitivity of the spectral effects to AOD was examined, assuming a continental aerosol with AOD = 0, 0.06, and 0.6, TWV = 1.5 cm, and ozone amount = 350 DU. Since the effect is very small (< 0.2%) for low aerosol loading, we focus on the effect caused by moderately large aerosol amounts. The sensitivity of the spectral correction to aerosol for the red channel of AVHRR (relative to AVHRR/NOAA-9) is negligible for AVHRR/NOAA-8, -11, and -12 (Fig. 10). It may reach 2–3% for AVHRR/NOAA-6, -7, and -10 and exceed 3% for NOAA-15 and -16. The correction is negative for AVHRR/NOAA-14 (from − 1% to − 2%). The absolute magnitude of the correction ranges from − 0.001 to 0.002. The sensitivity is similar for other sensors (Fig. 10).

The sensitivity for NIR channels of AVHRR is even smaller in general (figures omitted; from − 0.3% to − 1%) and somewhat larger for MODIS, VGT, and GLI (from − 2% to − 5%) NIR channels. The magnitude of sensitivity of the NDVI spectral correction to AOD falls within − 3% and 3%. While such an effect is comparable with the instrument uncertainties, the effect is persistent for aerosol laden atmosphere and is thus recommended to be taken into consideration in intercomparison studies, if possible.

4.4.3. Ozone amount

The sensitivity of the spectral correction to ozone amount is studied for 270, 350, and 430 DU. Since ozone has a weak absorption in the visible region centered around 0.6 μm (*Chappius* band; Liou, 1992), the sensiti-

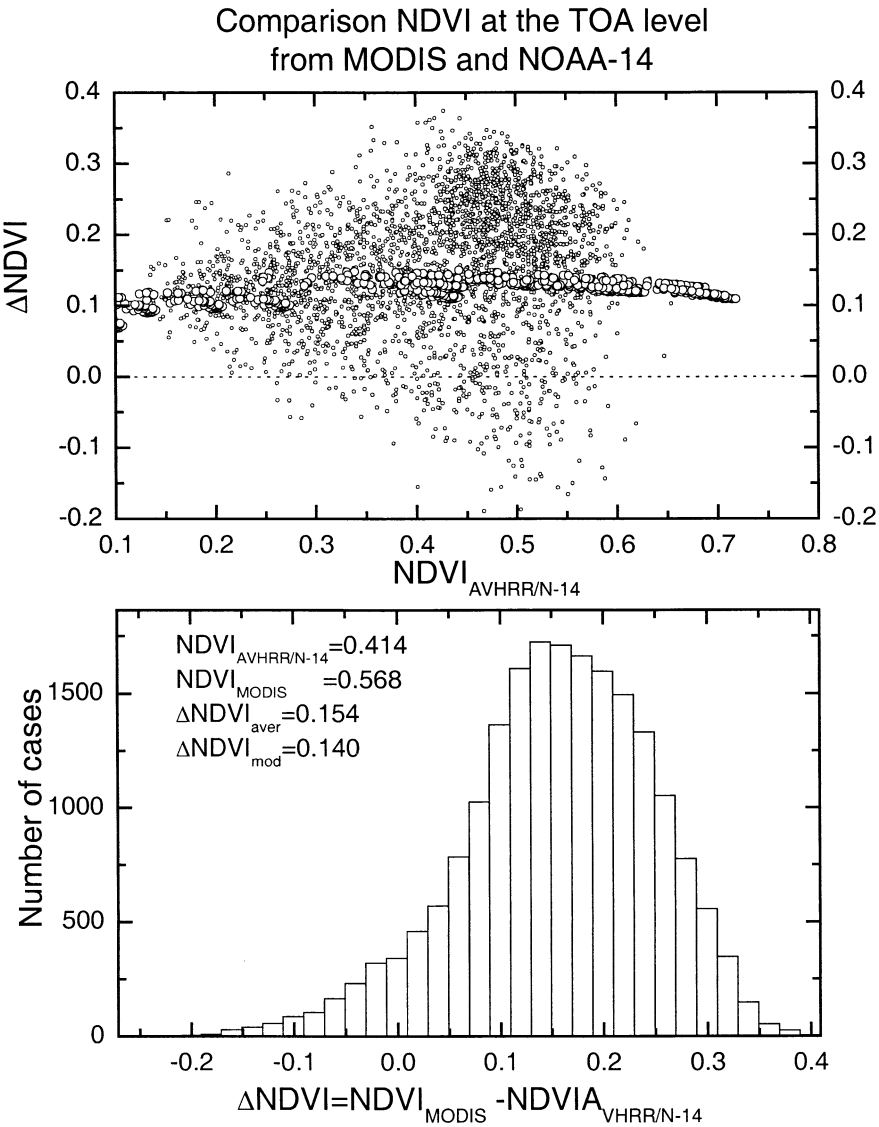

Fig. 12. Similar to Fig. 11, but for comparison of NDVI at the TOA level derived from MODIS and AVHRR/NOAA-14. Like in previous comparison, good agreement is found on average between modeling and observations both in the sign and magnitude of SRF effect. The scattering of observed points is due to possible residual cloud contamination and resampling of MODIS image from Integerized Sinusoidal Projection (ISP) to Lambert conformal conic projection, which alters the image resolution.

vity is overly small. For all AVHRRs and MODIS, the correction is typically less than $\sim 0.5\%$ or 0.001 in absolute units. For VGT and GLI, the effect is slightly larger, 0.5–1% relative or 0.002 absolute. The magnitude of the ozone effect on the NDVI spectral correction is equally small, as it essentially affected by changes in visible reflectances only.

5. Application to real satellite data

To test the modeling results, we compared two pairs of images over identical areas. One pair is for AVHRR images acquired by NOAA-14 and -15 and another pair is for AVHRR/NOAA-14 and MODIS. The images in each pair were taken very close in time so that temporal changes do not affect the comparisons. Two AVHRR images were taken over an area of Northern Ontario (Canada) observed on July 15, 2000 in the morning (NOAA-15) and afternoon (NOAA-14). The area is approximately 250×250 km centered around (53°N, 87.5°W).

The second comparison is between clear-sky composites from MODIS and AVHRR/NOAA-14 over an area of Southern Great Plains (USA). MODIS covers the period July 19–26, 2000 and the AVHRR for the period July 21–31, 2000. All images were resampled to Lambert conformal conic projection with 1-km resolution. The area of comparison is $10 \times 8°$ centered around (36°N, 97°W). Joint statistical distributions of reflectances and brightness temperatures were analysed and additional thresholds were applied to all images to detect and to remove cloud-contaminated pixels in addition to clear-sky compositing procedures. Water pixels were excluded from the comparison due to strong directional effects that would complicate the comparison (Cihlar et al., in press). The directional effects resulting from different local observation times and geometry do exist over land as well (Li et al., 1996) but less pronounced than water bodied. The effect is further reduced for NDVI due to considerable cancellation of the effects in the visible and NIR channels (Gutman, 1999; Li et al., 1996).

The comparisons of NDVI between AVHRR/NOAA-14 and -15 and between AVHRR/NOAA-14 and MODIS are presented in Figs. 11 and 12. Statistical analyses using the *t* test showed that the two comparisons have statistically significant nonzero mean difference at a significance level .01 or lower. The modal value of the distribution of NDVI differences between AVHRR/NOAA-15 and AVHRR/NOAA-14 shown in Fig. 11 is 0.025 or 5.7%. The difference between average values is slightly smaller (0.017 or 3.9%) because of skewness of the distribution. This difference is in conformity with modeling results, which also indicate a greater magnitude of NDVI for AVHRR/NOAA-15 than for AVHRR/NOAA-14. The magnitude of differences between modeled NDVIs is slightly larger (1.4%) due to contributions by various factors, in particular due to aerosol and surface directional effects.

The directional effect is lessened for the comparison between MODIS and AVHRR/NOAA-14 due to closer observation times (Fig. 12). The observed modal value of the NDVI difference is 0.14 (29%) and the mean difference of 0.15 (31%), in comparison with the modeled NDVI difference of about 0.125 (25%). Slightly smaller values of NDVI difference for the modeling case may reflect the contribution of water vapor effect, as discussed in Section 4. Good overall agreement between modeling estimates and satellite observations bolsters our confidence in the estimates of spectral correction effects derived in this paper.

6. Conclusions

Long-term monitoring of the Earth's environment by satellite sensors require consistent and comparable measurements. In this paper, we evaluated the effect of a major sensor parameter, namely, the SRF, on the consistency of observations made by moderate resolution sensors commonly used for surface and atmospheric studies. Starting with TIROS-N in 1978, these sensors have provided a long time series of satellite data, which contain rich information pertaining to the state and changes of many important environmental and meteorological variables. However, use of such diverse data sets requires a careful evaluation of their compatibility and consistency to avoid any artifact. This study elaborates the influence of different SRF on reflectance measurements in the visible and NIR channels and on their combination in the form of NDVI. The sensors under study include AVHRRs from NOAA-6 to the latest NOAA-16 as well as MODIS, VGT, and GLI. All the sensors are compared to the AVHRR/NOAA-9, which was chosen as a reference.

The study illustrated that the differences in SRF are significant enough to be taken into account, in particular for studies concerning interannual variations. It is comparable in magnitude to the uncertainties caused by sensor calibration and the angular correction procedure. Even among "the same type" instruments such as AVHRR, the effect of the varying SRF on surface and TOA spectral reflectances and NDVI vegetation index is sufficiently large to require correction. Relative to the AVHRR/NOAA-9, differences range from -25% to 12% for visible reflectance (red) and from -2% to 4% for NIR reflectance. The absolute differences in NDVI among various AVHRRs range from -0.02 to 0.06. The most consistent with AVHRR/NOAA-9 results were obtained for AVHRR/NOAA-11 and -12 where the corrections are small and optional. The corrections must be implemented for other AVHRRs and especially for the AVHRR/3 on NOAA-15 and -16. Reflectances and NDVI from MODIS differ from AVHRR/NOAA-9 by as much as 30–40%. Likewise, VGT and GLI also exhibit considerable differences relative to AVHRR observations.

Given the significant effect of SRF, simple polynomial approximations were derived that may be used for correc-

tion. They provide a good accuracy of approximation for the AVHRR sensors. Other sensors (MODIS, VGT, and GLI) require more significant correction to adjust for spectral differences in comparison with AVHRR. Polynomial approximations, we propose for these sensors, may be used as first-order corrections. Higher accuracy may be achieved by taking into consideration the atmospheric variables, observational angles, and information from additional spectral channels available from these instruments (Gitelson & Kaufman, 1998).

Sensitivity tests of the SRF effect to various atmospheric variables (water vapor, aerosol, and ozone) were conducted. In general, their influences are rather small. The largest effect is caused by aerosol, which may reach a few percent. Water vapor affects the spectral correction between AVHRR and other sensors but not within AVHRR modifications. Ozone variation generally exerts a small effect for all sensors and may be neglected. The effects of SRF are further reinforced by analyses of two pairs of real satellite imagery data for AVHRR from NOAA-14 and -15 and from MODIS. The observational results are generally in good agreement with model simulations both in sign and magnitude of the SRF effect.

Acknowledgments

Authors are grateful to J.-C. Deguise and R. Hitchcock of CCRS for making PROBE-1 data available for this study. We acknowledge the use of spectral data from JPL ASTER spectral library (http://speclib.jpl.nasa.gov). The authors also thank Gunar Fedosejevs for his valuable comments and discussion. This research was partially supported by the Biological and Environmental Research Program (BER), U.S. Department of Energy, Grant No. DE-FG02-02ER63351.

References

Bannari, A., Morin, D., & Bonn, F. (1995). A review of vegetation indices. *Remote Sensing Reviews*, *13*, 95–120.

Brest, C. L., Rossow, W. B., & Roiter, M. D. (1997). Update of radiance calibrations for ISCCP. *Journal of Atmospheric and Oceanic Technology*, *14*, 1091–1109.

Chen, J. M., Rich, P. M., Gower, T. S., Norman, J. M., & Plummer, S. (1997). Leaf area index of boreal forests: theory, techniques and measurements. *Journal of Geophysical Research*, *102*, 29429–29444.

Cihlar, J., Chen, J. M., Li, Z., Huang, F., Latifovic, R., & Dixon, R. (1998). Can interannual land surface signal be discerned in composite AVHRR data. *Journal of Geophysical Research*, *103*, 23163–23172.

Cihlar, J., Latifovic, R., Chen, J., Trishchenko, A., Du, Y., Fedosejevs, G., & Guindon, B. (2001). Systematic corrections of AVHRR image composites for temporal studies. *Remote Sensing of Environment (Accepted, August 2001)*.

Cihlar, J., Tcherednichenko, I., Latifovic, R., Li, Z., & Chen, J. (2000). Impact of variable atmospheric water vapor content on AVHRR data corrections over land. *IEEE Transactions on Geoscience and Remote Sensing*, *39* (1), 173–180.

Cracknell, A. P. (1997). *The advanced very high resolution radiometer (AVHRR)* (534 pp.). London: Taylor & Francis.

Csiszar, I., Gutman, G., Romanov, P., Leroy, M., & Hautecoeur, O. (2001). Using ADEOS/POLDER data to reduce angular variability of NOAA/AVHRR reflectances. *Remote Sensing of Environment*, *76*, 399–409.

Fedosejevs, G., O'Neill, N., Royer, A., Teillet, P. M., Bokoye, A. I., & McArthur, B. (2000). Aerosol optical depth for atmospheric correction of AVHRR composite data. *Canadian Journal of Remote Sensing*, *26*, 273–284.

Gitelson, A., & Kaufman, Y. J. (1998). MODIS NDVI optimization to fit the AVHRR data series — spectral consideration. *Remote Sensing of Environment*, *66*, 343–350.

Gobron, N., Pinty, B., Verstraete, M. M., & Widlowski, J.-L. (2000). Advanced vegetation indices optimized for up-coming sensors: design, performance, and applications. *IEEE Transactions on Geoscience and Remote Sensing*, *38* (6), 2489–2505.

Gutman, G. (1999). On the use of long-term global data of land reflectances and vegetation indices derived from the advanced very high resolution radiometer. *Journal of Geophysical Research*, *104* (6), 6241–6255.

Gutman, G., Csiszar, I., & Romanov, P. (2000). Using NOAA/AVHRR products to monitor El Niño impacts: focus on Indonesia in 1997–98. *Bulletin of the American Meteorological Society*, *81*, 1189–1205.

Gutman, G., Gruber, A., Tarpley, D., & Taylor, R. (1989). Application of angular models to AVHRR data for determination of the clear-sky planetary albedo over land surfaces. *Journal of Geophysical Research*, *94*, 9959–9970.

Hucek, R., & Jacobowitz, R. (1995). Impact of scene dependence on AVHRR albedo models. *Journal of Atmospheric and Oceanic Technology*, *12* (4), 697–711.

Kaufman, R. K., Zhou, L., Knyazikhin, Y., Shabanov, N. V., Myneni, R. B., & Tucker, C. J. (2000). Effect of orbital drift and sensor changes on the time series of AVHRR vegetation index data. *IEEE Transactions on Geoscience and Remote Sensing*, *38* (6), 2584–2597.

Kidwell, K. (1994). *Global vegetation index user's guide*. U.S. Dept. of Commerce, NOAA/National Environmental Satellite Data and Information Service, National Climatic Data Center, Satellite Data Services Division, Suitland, MD 20746.

Li, Z., Cihlar, J., Zheng, X., Moreau, L., & Ly, H. (1996). The bidirectional effects of AVHRR measurements over boreal regions. *IEEE Transactions on Geoscience and Remote Sensing*, *34*, 1308–1322.

Li, Z., Moreau, L., & Cihlar, J. (1997). Estimation of photosynthetically active radiation absorbed at the surface. *Journal of Geophysical Research*, *102*, 29717–29727.

Li, Z., Nadon, S., & Cihlar, J. (2000). Satellite detection of Canadian boreal forest fires: development and application of an algorithm. *International Journal of Remote Sensing*, *21*, 3057–3069.

Liou, K. N. (1992). *Radiation and cloud processes in the atmosphere: theory, observation, and modeling*. New York: Oxford University Press.

Masonis, S. J., & Warren, S. G. (2001). Gain of the AVHRR visible channel as tracked using bidirectional reflectance of Antarctic and Greenland snow. *International Journal of Remote Sensing*, *22*, 1495–1520.

Nakajima, T., Higurashi, A., Kawamoto, K., & Penner, J. E. (2001). A possible correlation between satellite-derived cloud and aerosol microphysical parameters. *Geophysical Research Letters*, *28*, 1171–1174.

Qin, Z., & Karnieli, A. (1999). Progress in the remote sensing of land surface temperature and ground emissivity using NOAA-AVHRR data. *International Journal of Remote Sensing*, *20*, 2367–2393.

Rao, C. R. N., & Chen, J. (1999). Revised post-launch calibration of the visible and near-infrared channels of the Advanced Very High Resolution Radiometer (AVHRR) on the NOAA-14 spacecraft. *International Journal of Remote Sensing*, *20*, 3485–3491.

Reynolds, R. W., & Smith, T. M. (1993). Improved global sea surface temperature analysis using optimum interpolation. *Journal of Climate*, *7*, 929–948.

Rossow, W. B. (1989). Measuring cloud properties from space: a review. *Journal of Climate*, *2*, 201–213.

Rossow, W. B., & Schiffer, R. A. (1999). Advances in understanding clouds from ISCCP. *Bulletin of the American Meteorological Society*, *80*, 2261–2287.

Rutan, D., & Charlock, T. P. (1997). Spectral reflectance, directional reflectance, and broad-band albedo of the Earth's surface. In: *Proc. 9th conference on atmospheric radiation, Long Beach, California*, (pp. 466–470). Boston, MA: American Meterological Society.

Secker, J., Staenz, K., Budkewitsch, P., & Neville, R. A. (1999). A vicarious calibration of the Probe-1 hyperspectral sensor. In: *4th International airborne remote sensing conference and exhibition/ 21st Canadian symposium on remote sensing* (pp. 21–24, 75–82). Ottawa, Ontario, Canada, Ann Arbor, MI, USA: ERIM International Inc. (June).

Stowe, L. L., Ignatov, A. M., & Singh, R. R. (1997). Development, validation, and potential enhancements to the second-generation operational aerosol product at the National Environment Satellite, Data, and Information Service of the National Oceanic and Atmospheric Administration. *Journal of Geophysical Research*, *102*, 16923–16934.

Tahnk, W. R., & Coakley, J. A. (2001). Updated calibration coefficients for NOAA-14 AVHRR channels 1 and 2. *International Journal of Remote Sensing*, *22* (15), 3053–3057.

Teillet, P. M., Barker, J., Markham, B. L., Irish, R. R., Fedosejevs, G., & Storey, J. C. (2001). Radiometric cross-calibration of the Landsat-7 ETM+ and Landsat-5 TM sensors based on tandem data sets. *Remote Sensing of Environment*, *78*, 39–54.

Teillet, P. M., Staenz, K., & Williams, D. J. (1997). Effects of spectral, spatial, and radiometric characteristics on remote sensing vegetation indices of forested regions. *Remote Sensing of Environment*, *61*, 139–149.

Trishchenko, A. P., Li, Z., Park, W., & Cihlar, J. (2001). Corrections for the BRDF and topographic effects in satellite retrieval of surface spectral reflectance in solar spectral region. In: W. L. Smith, & Y. Tymofeyev (Eds.), *Proc. of the Int. Radiation Symp. IRS 2000. St. Petersburg, Russia, August 2000*, *vol. 147* (pp. 44–47). Hampton, VA, USA: A. Deepak Publishing.

Vermote, E., Tanré, D., Deuzé, J. L., Herman, M., & Morcette, J. J. (1997). Second simulation of the satellite signal in the solar spectrum: an overview. *IEEE Transactions on Geoscience and Remote Sensing*, *35*, 675–686.